Arabian Journal for Science and Engineering
https://doi.org/10.1007/s13369-024-09149-5

RESEARCH ARTICLE-CIVIL ENGINEERING

Fatigue Evaluation of Sulphate-Attacked Industrial Waste-Based Concrete Using Concrete Damaged Plasticity Model

Matthew Zhi Yeon Ting[1,2] · Kwong Soon Wong[1] · Muhammad Ekhlasur Rahman[1,3] · Meheron Selowara Joo[1]

Received: 17 December 2023 / Accepted: 30 April 2024

Abstract
Sulphate attack is a major cause of concrete deterioration in marine environments and its interaction with wave-induced cyclic loading exacerbates the damage. This study has evaluated strengths and fatigue performance (i.e. fatigue life, strain and residual displacement) of sulphate-attacked concrete containing silicomanganese slag, fly ash (FA) and silica fume (SF). Compressive strength, tensile strength and sulphate profile of sulphate-attacked concrete were measured experimentally. Sulphate-induced damage constitutive relations were formulated and used with concrete damaged plasticity (CDP) model to simulate fatigue loading. Experiment showed that incorporating silicomanganese slag lowered sulphate resistance by 4.8–6.6% due to increased sulphate intrusion, but synergy with FA and SF enhanced the resistance by 7.3–13.8% at 365 days. The sulphate penetration depth was 0–20 mm, and the intruded sulphate increased exponentially over time. To evaluate fatigue loading in CDP model, the non-uniform damage was determined as correlation between strength degradation and integral area of sulphate profile. Numerical results were in good agreement with experimental data from literature, with differences of 5.8–26.2% in fatigue life, 9.1–30.1% in fatigue strain and 18.1–41.9% in residual displacement. In long-term deterioration, numerical analysis found that increasing sulphate concentration significantly shortened fatigue life. Despite silicomanganese slag lowered concrete sulphate and fatigue resistance, the inclusion of FA and SF improved the durability and sustainability of concrete for potential marine applications.

Keywords Concrete · Deterioration · Fatigue life · Sulphate attack · Wetting–drying cycle

1 Introduction

Sulphate attack is a primary cause of deterioration in concrete structures exposed to marine environment [1–3]. Sulphate from seawater can permeate concrete pores by capillary absorption and diffusion, causing chemical and physical damages. Chemically, sulphate interacts with cement hydrates such as calcium aluminate hydrate (C–A–H) and calcium hydroxide ($Ca(OH)_2$) to form degradation products such as ettringite and gypsum [4, 5]. Sulphate attack degrades calcium silicate hydrate (C–S–H) gels, reducing mechanical strength. The depletion of $Ca(OH)_2$ also reduces the alkalinity in pore solution and diminishes the corrosion resistance of reinforced concrete. Physically, the production of ettringite and gypsum within concrete pores causes damage through expansion. These deterioration products have an expansion ratio of 2–3, which can result in mortar spalling and concrete cracking [6, 7].

Existing studies utilize several metrics to evaluate the sulphate resistance of concrete. The majority of research [8–10] focuses on measuring the mass change of concrete due to the potential development of ettringite and breakdown of hydrates caused by sulphate attack. However, mass

✉ Kwong Soon Wong
wongkwongsoon@curtin.edu.my

Matthew Zhi Yeon Ting
matthewzhiyeon.ting@ntu.edu.sg

Muhammad Ekhlasur Rahman
muhammad2.rahman@northumbria.ac.uk

Meheron Selowara Joo
meheron.sj@curtin.edu.my

1 Department of Civil and Construction Engineering, Faculty of Engineering and Science, Curtin University Malaysia, CDT 250, 98009 Miri, Sarawak, Malaysia

2 School of Civil and Environmental Engineering, Nanyang Technological University, Singapore 639798, Singapore

3 Faculty of Engineering and Environment, Northumbria University, Newcastle Upon Tyne, UK

Published online: 29 May 2024

change is often mistaken for water absorption and hydration. Some studies [8, 10, 11] employ the relative dynamic modulus of elasticity (RDME) as a means of assessing concrete degradation. The RDME refers to the elasticity under longitudinal vibration and may not accurately represent the extent of damage. Compressive strength is by far the most reliable metric for assessing concrete deterioration because it portrays the ultimate limit state [8–10, 12–14]. Besides, there has been limited study regarding the tensile strength of concrete subjected to sulphate attack. Tensile strength has an important function in resisting concrete cracks and should be further investigated. In addition, sulphate penetration profile is another reliable indication of sulphate attack and should be assessed [5, 7].

To account for concrete in-service conditions, past studies [11, 15–17] have combined sulphate attack with external loadings. Gao et al. [11] found that coupling with 20–40% flexural loading had minimal effect, but increasing to 60% loading considerably accelerated sulphate deterioration owing to generation of micro-cracks. Chen et al. [15] demonstrated that the degradation induced by long-term flexural loading was nearly double that of short-term loading. According to Fu et al. [17], applying 25–45% uniaxial tensile loading caused permanent damage in terms of concrete cracking and increased intrusion of corrosive ions. Zhang et al. [16] showed that tensile loading also caused stiffness degradation, reducing its sulphate resistance. Nevertheless, marine structures such as breakwaters, seawalls and offshore platforms are often subjected to wave action that is neither flexural nor tensile. Wave loading usually takes the form of hydrodynamic drag force and impact load [18], which results in primarily compressive loading. However, the available research lacks information on the combined compressive loading and sulphate attack. Although concrete is considered robust in compression, compressive loading in cyclic form, such wave action, can cause significant progressive damage, necessitating further study.

Sulphate attack and cyclic loading are long-term processes that occur independently. Sulphate attack is physicochemical deterioration process, whereas cyclic loading causes physical fatigue damage. According to the literature [8, 11, 15, 16, 19], sulphate attack causes degradation over months to years, depending on concrete grade, mixture additive, permeability, sulphate concentration and exposure conditions. Wave-induced cyclic loading normally is of low magnitude and will take considerably longer to cause damage. Studies [20, 21] have found that concrete only shows evidence of damage after 50 years of wave activity; hence, sulphate deterioration may have happened. Thus, to simplify the interactions, it is reasonable to assume that sulphate attack causes concrete deterioration first, followed by cyclic loading.

Several research works [22–24] reported detrimental effect of sulphate attack on concrete fatigue resistance. Long et al. [22] showed that sulphate attack reduced fatigue life (ln N) of concrete under flexural loading by 1–4 orders of magnitude. According to Biswas et al. [23], the seismic resistance of concrete bridge was compromised by sulphate attack with the spalling of concrete cover, confinement loss and lower load carrying capacity. Flansbjer et al. [24] found that 40 years of sulphate attack reduced the load carrying capacity of concrete piles by 15%, weakening their dynamic resistance. According to the literature review, there has been little research on the fatigue behaviour of sulphate-attacked concrete, especially under cyclic compressive loading; hence, further research is needed.

Fatigue loading test requires significant experimental effort and time. Concrete has heterogeneous properties that are sensitive to loading conditions, often leading to inconsistent results. Hence, numerical method, such as concrete damaged plasticity (CDP) model, may be used to evaluate fatigue performance. CDP defines non-linear concrete damage and offers effective dilatancy control to simulate fatigue [25]. CDP also incorporates stiffness recovery parameters to account for cracks opening and closing in cyclic loading [26]. Several researches have employed CDP model for concrete cyclic loading. Azadi Kakavand and Taciroglu [27] showed that CDP model could capture cyclic behaviour across full range of compressive loads up to compressive strength. Minh et al. [28] demonstrated that adjusting the biaxial-to-uniaxial compression ratio in CDP model accurately simulated the dynamic behaviour of high-strength concrete over a strength range of 60–110 MPa. Murthy et al. [29] used the CDP model with pre-damage factor to evaluate fatigue behaviour of concrete beam under 70–90% pre-loaded conditions. Therefore, CDP model may be used to simulate the fatigue behaviour of sulphate-attacked concrete.

Considering the existing research, only a limited investigation has been conducted to assess the compressive fatigue resistance of concrete subjected to sulphate attack. To reduce cost and time, the study can be performed numerically using the CDP model. Hence, this research work aims to perform a numerical study on fatigue resistance of sulphate-attacked concrete. Experiments were conducted to determine damage constitutive relations of sulphate-attacked concrete in terms of compressive strength, tensile strength and sulphate intrusion. The fatigue loading of concrete was modelled by using the CDP model in ABAQUS.

2 Experiment

2.1 Materials and Mix Proportions

The binders used in this study included 42.5 N ordinary Portland cement (OPC), fly ash (FA) and silica fume (SF). FA and SF were added to improve sulphate resistance of concrete

[30–32]. The performance of two types of coarse aggregate, limestone and silicomanganese slag, was compared. Silicomanganese slag was industrial byproduct generated during the smelting of ferroalloys in steel production, and its incorporation into concrete could improve sustainability [33, 34]. The specific gravity of limestone and silicomanganese slag was 2.64 and 2.97, the fine modulus was 6.97 and 7.67, and the abrasion resistance was 22% and 12%, respectively. For fine aggregate, marine sand was blended with quarry dust, yielding a mixture having specific gravity of 2.7 and fineness modulus of 2.59. Sulphonated-naphthalene formaldehyde type superplasticizer (SP) was used to improve concrete workability.

Table 1 summarizes the mix proportions of four concrete types investigated. The mixtures incorporated with silicomanganese slag aggregate were labelled as SM and SM:(SF + FA). SM was reference mix containing OPC, and SM:(SF + FA) was mix containing OPC, FA and SF. The FA and SF replacement levels were selected based on the optimization in the past study [35]. Concrete with limestone as coarse aggregate was included for comparison, denoted as LS and LS:(SF + FA). All concrete mixes had a water-to-binder content (W/B) ratio of 0.32 and an SP content of 1%.

2.2 Specimen Preparation and Test Method

Concrete specimens were casted and demoulded after 1 day. The specimens were cured in water for 165 days to minimize hydration effect on test results. After curing, concrete was exposed to wetting–drying process based on the local tidal phenomena (Tanjung Lobang Beach, Malaysia). The wetting–drying process included soaking in salt solution for 12 h and air-drying at room temperature (27 °C) for 11 h. The process also took 0.75 h to remove solution and 0.25 h to refill it. Sodium sulphate (Na_2SO_4) solutions with concentrations of 5% (E1), 12.5% (E2) and 20% (E3) were used. The total wetting–drying periods were 365 days, with the Na_2SO_4 solutions being refreshed every 30 days. Three specimen replicates were prepared for all tests performed. Figure 1 illustrates schematic diagram of specimen preparation and test setup.

2.2.1 Compressive Strength Test

Compressive strength test was carried out on 100 mm cube specimens using 3000 kN compression testing equipment. The compression test was conducted in reference to the ASTM C39 standard [36]. The compressive strength of concrete was measured after 0, 30, 60, 90, 120, 150 and 365 days of sulphate attack.

2.2.2 Tensile Strength Test

Splitting tensile test was conducted on cylindrical specimens of 100 mm diameter and 200 mm height. The tensile strength test was tested in accordance with the ASTM C496 standard [37]. The splitting tensile strength was measured after 0, 30, 60, 90, 120, 150 and 365 days of sulphate attack.

2.2.3 Sulphate Ion Penetration

The penetration of sulphate (SO_4^{2-}) ions was measured on 75 × 75 × 300 mm prisms. By drilling the specimen along penetration path, powder samples were collected from the concrete depths of 0–5 mm, 5–10 mm, 10–15 mm and 15–20 mm. The SO_4^{2-} content was measured using the barium sulphate gravimetric method described in the ASTM C114 standard [38]. The deterioration of sulphate-attacked concrete was not uniform across the specimen, with deterioration decreased as the depth increased. Therefore, in order to accurately express the deterioration process, the integral area of SO_4^{2-} distribution was evaluated and was used in the analysis of this study [7].

3 Experimental Results and Discussion

3.1 Compressive Strength

Figure 2 depicts concrete compressive over the period of sulphate attack. The strength generally decreased with exposure time. It was known that the primary source of strength deterioration during sulphate attack was the expansion damage from ettringite formations [6, 7]. Sulphate reactions also consumed cement hydrates and induced dissolution of $Ca(OH)_2$, C–A–H and C–S–H [4, 5]. In this study, the presence of WDA resulted in damages associated with salt crystallization and drying shrinkage.

Figure 2a compares the compressive strength of all mixes exposed to E3 (20% Na_2SO_4). LS concrete showed less strength reduction than SM concrete. At 365 days, LS lost 36–41% of its strength compared to 39–45% for SM. The greater strength loss of SM concrete might be attributed to three reasons. First, SM aggregate had flakier and smoother surface compared to LS aggregate, which resulted in weaker bond with cementitious paste, leading to increase in sulphate intrusion [39]. Second, SM aggregate exhibited 45.5% lower abrasion resistance than LS aggregate, producing concrete with weaker mechanical properties. Xing et al. [40] also discovered that the crushing strength of SM aggregate was 43–50.8% lower than that of LS aggregate. Third, the presence of alumina content in SM aggregate might react with sulphate ions to accelerate the deterioration [41]. Nonetheless, the use of FA and SF as supplementary materials could

Table 1 Mix proportions of concrete

Mix description	OPC (kg/m^3)	FA (kg/m^3)	SF (kg/m^3)	CA1 (kg/m^3)	CA2 (kg/m^3)	Marine sand (kg/m^3)	Quarry dust (kg/m^3)	Water (kg/m^3)	SP (kg/m^3)
LS	550	0	0	965	0	515	173	176	5.5
LS:(SF + FA)	406	54	90	965	0	501	168	176	5.5
SM	550	0	0	0	1115	515	173	176	5.5
SM:(SF + FA)	406	90	54	0	1115	501	168	176	5.5

CA1 = Limestone; CA2 = Silicomanganese slag

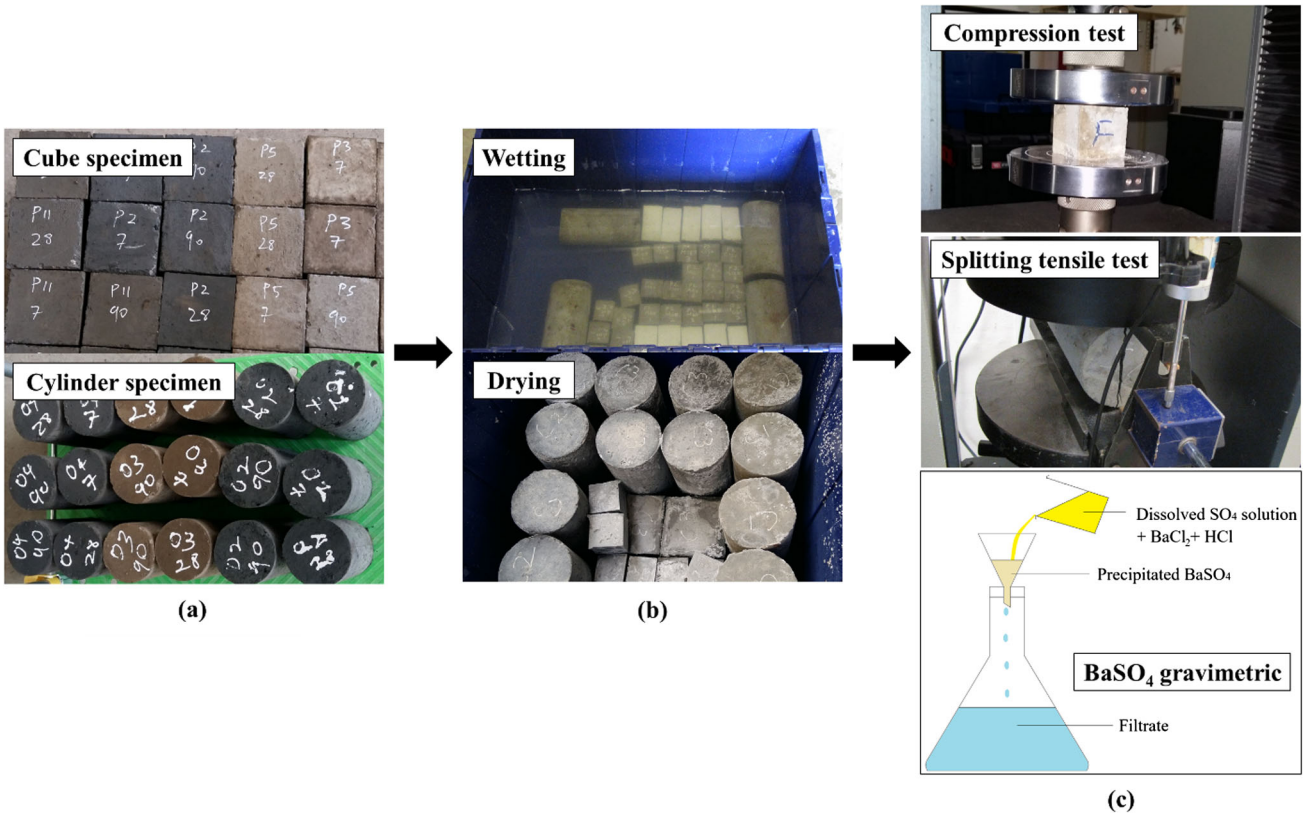

Fig. 1 Schematic diagram of experiment: **a** casted specimens, **b** wetting–drying process and **c** conducted tests

improve sulphate resistance, offsetting the drawback of SM concrete. As shown in Fig. 2a, the strength of SM:(SF + FA) was higher than that of LS. From 30 to 365 days, both mixtures showed comparable strengths, with degradation ratio (compared to 0-day sulphate attack) of 0.61–0.96 for SM:(SF + FA) and 0.56–0.98 for LS. This might be due to the pozzolanic reactions of FA and SF that consumed $Ca(OH)_2$, impeding the sulphate reactions. The production of additional C–S–H also densified concrete pore structure and reduced sulphate intrusion. El-Sayed and Shaheen [42] demonstrated that pozzolans with high silica and alumina contents created cementitious matrix with enhanced interparticle bonding, resulting in improved mechanical performance.

Figure 2b shows the compressive strength of LS under sulphate attack at three different solution concentrations: E1 (5% Na_2SO_4), E2 (12.5% Na_2SO_4) and E3 (20% Na_2SO_4). The increase in sulphate concentration caused a greater reduction in compressive strength. At 365 days, the strength loss was 16% in E1, 34% in E2 and 41% in E3. The 90-day strength loss in E3 was equivalent to 365-day strength loss in E1 and 120-day strength loss in E2. The sulphate deterioration process was accelerated with increased solution concentration. However, the strength degradation was not linearly proportional to the external sulphate concentration. Past studies [5, 7] showed that the internal sulphate content of concrete was a more representative parameter in

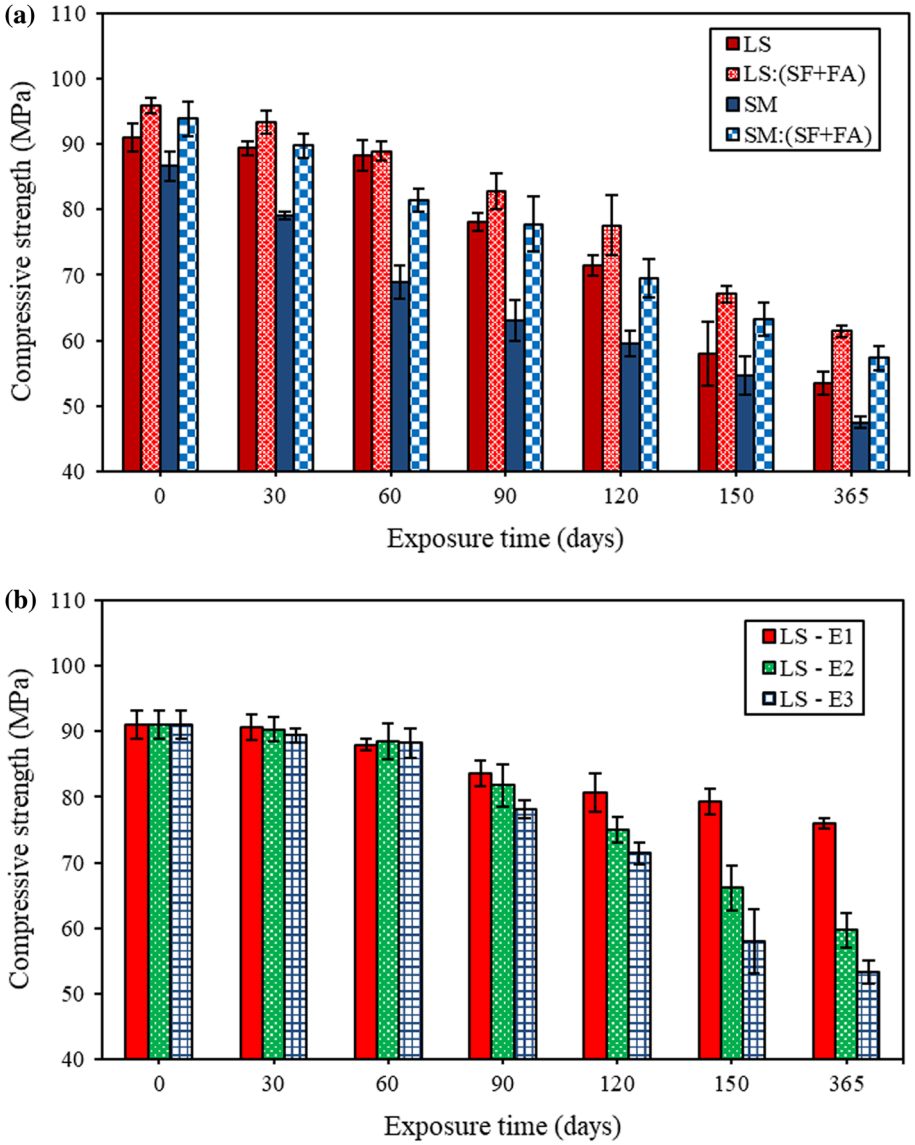

Fig. 2 Compressive strength of concrete: **a** all mixes in E3 (20% Na_2SO_4) and **b** LS in E1 (5% Na_2SO_4), E2 (12.5% Na_2SO_4) and E3 (20% Na_2SO_4)

assessing sulphate-related deterioration. Hence, the sulphate ion distribution was investigated further in Sect. 3.3.

3.2 Tensile Strength

Tensile strength of concrete exposed to sulphate attack is shown in Fig. 3. Similarly, the tensile strength decreased over exposure period. The tensile strength fell from 5.3–6.6 MPa at 0 day to 3.5–4.9 MPa at 365 days. When compared to compressive strength degradation, the tensile strength degradation was generally less severe. At 365 days, the tensile strength deterioration ratio was 0.67–0.83, which was higher than the compressive strength deterioration ratio of 0.55–0.82. This might be concrete under tension exhibited less internal stress induced by sulphate expansion products such as ettringite, gypsum and salt crystals. The result contradicted Tang et al. [10] finding that tensile strength degradation was higher than compressive strength. This could be ascribed to the lower strength concrete in that study, which could sustain limited tensile stress, showing more severe sulphate-induced tensile damages [43].

Figure 3a compares the tensile strength of all concrete types exposed to E3 (20% Na_2SO_4). Tensile strength loss of LS concrete was lower than that of SM concrete, with a difference of 1–17%. This was due to the flaky and slender characteristics of SM aggregate, as evidenced by a higher fineness modulus than LS aggregate, resulting in concrete with lower tensile resistance. According to Vishwakarma et al. [44], the gradation of coarse aggregate greatly affected its bonding with cementitious paste and hence tensile strength. Nevertheless, the incorporation of FA and SF reduced the strength loss caused by sulphate attack. As in

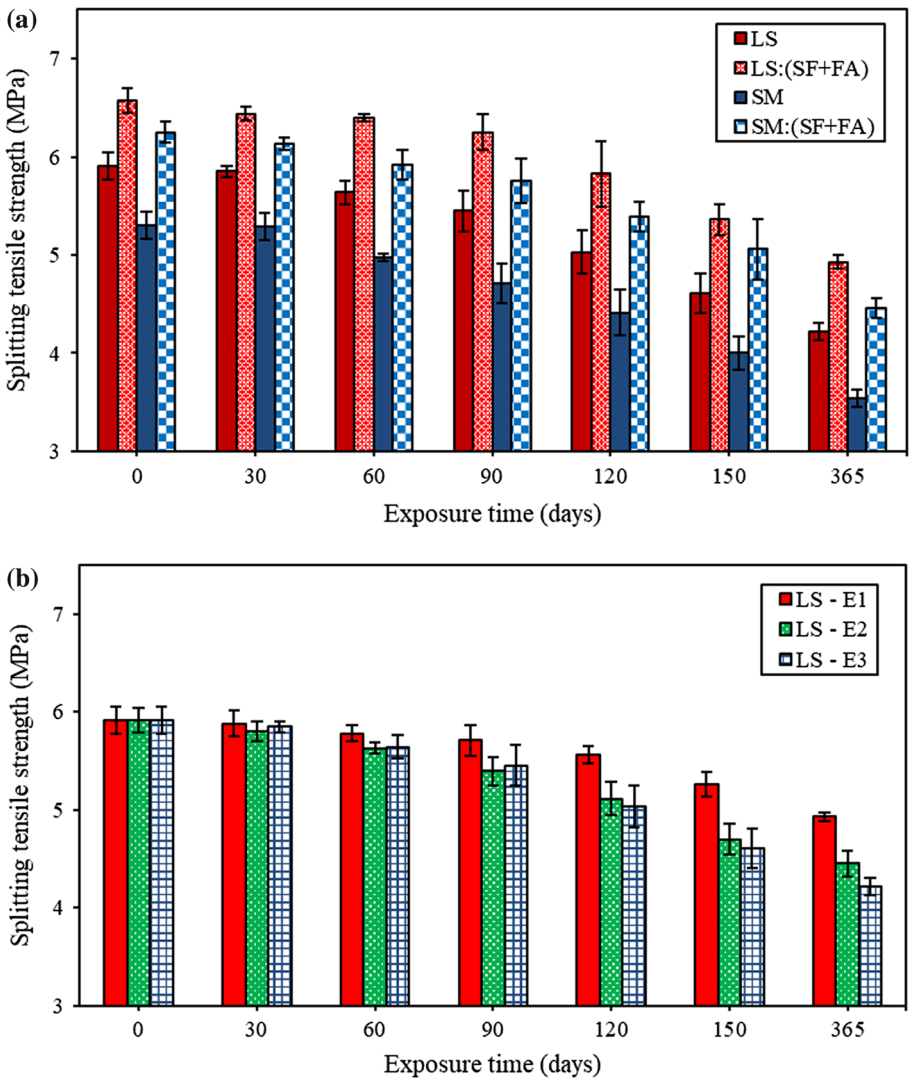

Fig. 3 Splitting tensile strength of concrete: **a** all mixes in E3 (20% Na_2SO_4) and **b** LS in E1 (5% Na_2SO_4), E2 (12.5% Na_2SO_4) and E3 (20% Na_2SO_4)

LS:(SF + FA) and SM:(SF + FA), the addition of FA and SF reduced the 365-day tensile strength loss by 3.6% and 4.5%, respectively, when compared to LS and SM. The pozzolanic reactions of FA and SF densified pore structure and minimized sulphate permeation.

Figure 3b depicts the variation in tensile strength of LS exposed to sulphate attack in three solution concentrations: E1 (5% Na_2SO_4), E2 (12.5% Na_2SO_4) and E3 (20% Na_2SO_4). An increase in sulphate concentration from 5 to 20% nearly doubled the tensile strength loss. For instance, at 365 days, the tensile strength deterioration ratio of LS was 0.83, 0.75 and 0.71 for concrete in E1, E2 and E3, respectively. In summary, the results of tensile strength corresponded well to those of compressive strength.

3.3 Sulphate Ion Penetration

The SO_4^{2-} content of concrete after sulphate attack was determined. Since concrete deterioration was not uniform across penetration depth, the integral area of SO_4^{2-} distribution was calculated for analysis [7]. Figure 4 depicts the variation of integral area of SO_4^{2-} distribution with exposure duration. The SO_4^{2-} content generally increased with exposure time. The rate of SO_4^{2-} penetration was higher in the early stage (0–150 days) compared to the later stage (150–365 days). At an early stage, concrete was in unsaturated state, and SO_4^{2-} transport was caused by absorption and diffusion. However, at a later stage, concrete became saturated, SO_4^{2-} penetration was attributed mostly to diffusion by concentration gradient and the rate dropped. Furthermore, Ikumi and Segura [6] also found that with increasing exposure time, more expansive products of ettringite and gypsum

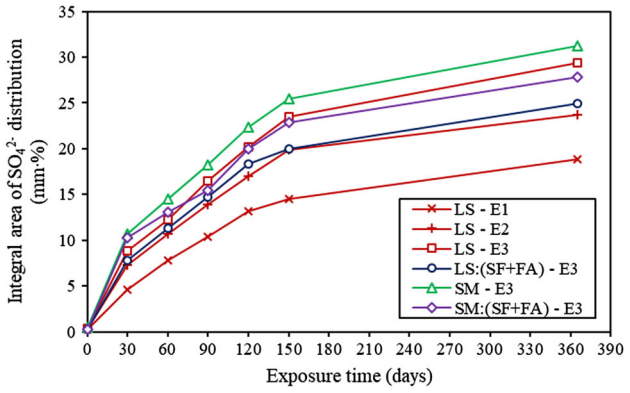

Fig. 4 Integral area of SO_4^{2-} distribution with exposure time

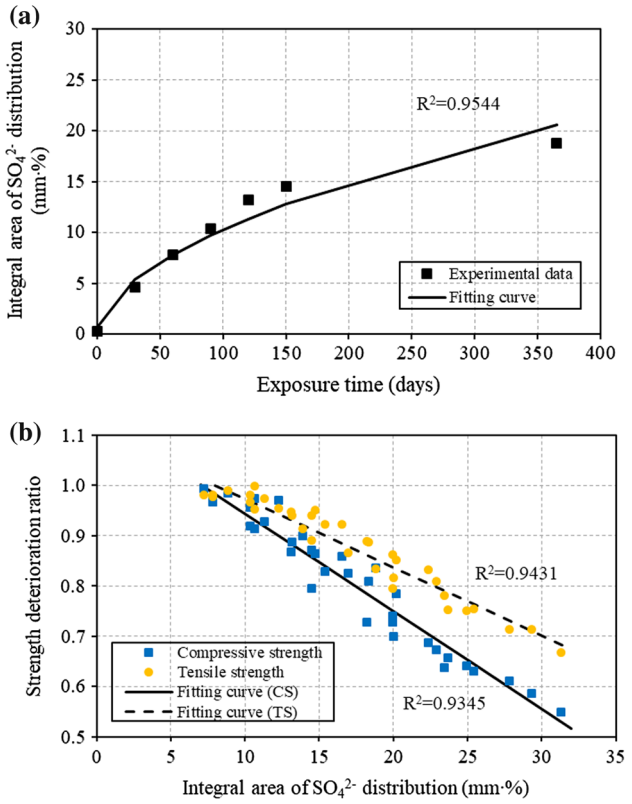

Fig. 5 **a** Non-linear fitting for integral area of SO_4^{2-} distribution and **b** correlation between integral area of SO_4^{2-} distribution and strength deterioration ratios

were generated to fill concrete pores, thus reducing sulphate intrusion.

When the mix types were compared, SM had slightly higher SO_4^{2-} content than LS. Besides, LS:(SF + FA) and SM:(SF + FA) had much less SO_4^{2-} content than LS and SM, with reductions of 15.1% and 10.9%, respectively, at 365 days. From microstructure viewpoint, the increase in corrosion resistance of concrete with FA and SF might be attributed to formation of denser gel structure. $Ca(OH)_2$ of cement hydrate was the key reactant in sulphate attack; therefore, pozzolanic reactions of FA and SF could convert it into C–S–H, enhancing sulphate resistance. Figure 4 also showed that the SO_4^{2-} content increased with solution concentration. The SO_4^{2-} content of LS in E3 was 1.2 and 1.6 times that of LS in E2 and E1, respectively. External sulphate solution with higher concentration increased the electrochemical gradient across the penetration depth, resulting in accelerated SO_4^{2-} diffusion.

4 Fatigue Loading Modelling of Sulphate-Attacked Concrete

4.1 Sulphate-Induced Deterioration

Sulphate attack resulted in non-uniform deterioration across concrete penetration depth. Based on the experiment, the deteriorated area extended from the concrete surface to a depth of 20 mm, where sulphate was primarily concentrated. Thus, the integral area of SO_4^{2-} distribution within this depth range was used to quantify the deterioration. Figure 5a showed that the integral area of SO_4^{2-} distribution increased with sulphate attack deterioration. Based on the experimental results in Sect. 3.3, the relationship between SO_4^{2-} and erosion duration was developed by using the non-linear fitting, as shown in Eq. (1). The fitting curve agreed well with the experimental data, with a coefficient of determination of 0.9544, indicating that the relationship could reasonably predict the internal SO_4^{2-} content of sulphate-attacked concrete.

$$C_s(t) = 0.87e^{0.5374\ln(t)}k(0.04C_o + 0.8067) \quad (1)$$

where C_s is integral area of SO_4^{2-} distribution, C_o is concentration of sulphate solution, t is erosion duration and k is constant of concrete type ($k = 1$ for LS concrete, 1.1 for SM concrete and 0.97 for SF + FA concrete).

The internal SO_4^{2-} content and strength deterioration showed an interrelated pattern. The formulations of relationship between the integral area of SO_4^{2-} distribution and strength deterioration ratio were established using regression analysis, as illustrated in Fig. 5b. The equations for assessing the strength deterioration were expressed as linear functions, as shown in Eq. (2) for compressive strength and Eq. (3) for tensile strength.

$$d_{sa,c} = -0.0194C_s + 1.1375 \quad (2)$$

$$d_{sa,t} = -0.0136C_s + 1.1089 \quad (3)$$

where $d_{sa,c}$ and $d_{sa,t}$ are compressive and tensile strength deterioration ratios of sulphate-attacked concrete. The computed relationships had R^2 values of 0.9345 and 0.9431, respectively. The deterioration ratio of compressive and tensile strengths decreased linearly as the integral area of SO_4^{2-} distribution increased. The computed equations were employed in the following finite element model to consider the strength deterioration of sulphate-attacked concrete across penetration depth, representing the non-uniform deterioration.

4.2 Stress–Strain Curves and Damage Curves

An empirical model for uniaxial compression developed by Yang et al. [45] was used to generate compressive stress–strain in this study. The non-linear stress–strain behaviour of concrete was modelled as a parabolic curve, as defined in Eq. (4)–(6), with distinct β_1 values specified for ascending and descending branches.

$$f_c = \frac{(\beta_1 + 1)\frac{\varepsilon_c}{\varepsilon_o}}{\left(\frac{\varepsilon_c}{\varepsilon_o}\right)^{\beta_1} + \beta_1} f_c' \tag{4}$$

$$\beta_1 = 0.2e^{0.73\xi} \text{ for } \varepsilon_c \le \varepsilon_o \tag{5}$$

$$\beta_1 = 0.41e^{0.77\xi} \text{ for } \varepsilon_c \ge \varepsilon_o \tag{6}$$

where f_c is compressive stress, ε_c is compressive strain, $f_c{}'$ is peak stress, ε_o is strain that corresponds to peak stress and ξ is equal to $(f_c{}'/10)^{0.67}(2300/\rho_c)^{1.17}$ and ρ_c is concrete density. The experimental stress–strain curves were compared to those determined by the empirical model in Appendix 1, which demonstrated adequate accuracy of the empirical model.

The tension stiffening model developed by Nayal and Rasheed [46] and modified by Wahalathantri et al. [47] was used to generate tensile stress–strain curves, as shown in Fig. 6. In the model, the ascending curve was linear up to peak stress. The descending curve began with a drop in peak stress caused by crack initiation, which was followed by two segments of descending branch representing primary and secondary cracking.

The compressive and tensile behaviours of concrete in terms of damaged parameter (d) and inelastic strain (ε_{in}) were required in CDP model. The damaged parameter and inelastic strain were determined using Eq. (7) and (8), respectively. In order to check the validity of the calculated inelastic strain, the plastic strain (ε_{pl}) was determined using Eq. (9), whereby the plastic strain should increase with the inelastic strain. The input of compressive and tensile damage behaviours used in this study was presented in Appendix 2.

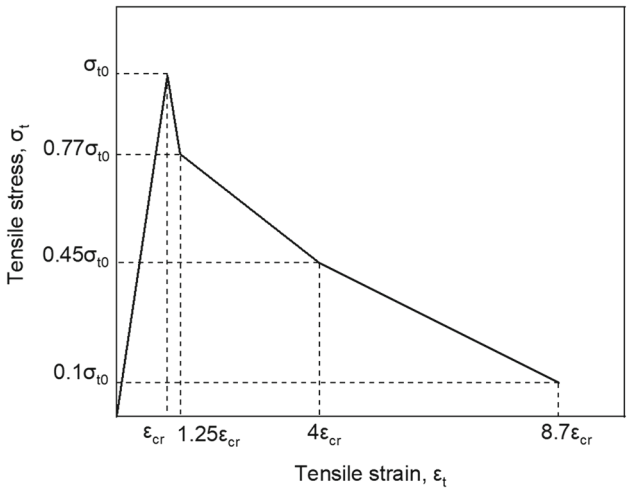

Fig. 6 Empirical tensile stress–strain curves [46, 47]

$$d = 1 - \frac{\sigma}{\sigma_{max}} \tag{7}$$

$$\varepsilon_{in} = \varepsilon - \frac{\sigma}{E_c} \tag{8}$$

$$\varepsilon_{pl} = \varepsilon_{in} - \frac{d}{1-d}\varepsilon_o \tag{9}$$

4.3 CDP Parameters

The CDP model in ABAQUS was developed based on plastic damage constitutive relations [26, 48]. The quasi-brittle behaviour of concrete could be modelled as beam, truss, shell and solid elements. The inelastic behaviour was described as damaged elasticity and isotropic plasticity. Equations (10) and (11) defined the stress tensor and damage parameter in the CDP model.

$$\sigma = (1 - d_c)\overline{\sigma} = (1 - d_c)E_o\left(\varepsilon - \varepsilon^{pl}\right) \tag{10}$$

$$(1 - d_c) = \left(1 - s_t d_{c,c}\right)\left(1 - s_c d_{c,t}\right) \tag{11}$$

where d_c is concrete damage parameter ranging from 0 to 1, $d_{c,c}$ and $d_{c,t}$ are damage parameter for compressive and tensile strengths, $\overline{\sigma}$ is effective stress, E_o is initial elastic modulus, ε and ε^{pl} are total strain and plastic strain and s_c and s_t. are compression and tension stiffness recovery factors.

The yield function in terms of effective stress is given in Eq. (12), which accounted for strength evolution under compression and tension. In the equation, $\overline{q}$ referred to Mises stress, $\overline{p}$ represented hydrostatic stress and $\overline{\sigma}_{max}$ was maximum principal stress. The parameter α was determined using

Eq. (13), where σ_{c0} and σ_{b0} were initial uniaxial and biaxial strengths. The parameter β was calculated using Eq. (14), where $\overline{\sigma}_c\varepsilon_c^{pl}$ and $\overline{\sigma}_t\varepsilon_t^{pl}$ were effective compression and tension cohesion stresses. The parameter γ was expressed as a function of tensile-to-compressive meridian ratio (K_c), as shown in Eq. (15), which defined the shape of yield surface.

$$F = \frac{1}{1-\alpha}\left(\overline{q} - 3\alpha\overline{p} + \beta\varepsilon^{pl}\overline{\sigma}_{\max} - \gamma - \overline{\sigma}_{\max}\right) - \overline{\sigma}_c\varepsilon_c^{pl} \tag{12}$$

$$\alpha = \frac{(\sigma_{b0}/\sigma_{c0}) - 1}{2(\sigma_{b0}/\sigma_{c0}) - 1} \tag{13}$$

$$\beta = \frac{\overline{\sigma}_c\varepsilon_c^{pl}}{\overline{\sigma}_t\varepsilon_t^{pl}}(1-\alpha) - (1+\alpha) \tag{14}$$

$$\gamma = \frac{3(1-K_c)}{2K_c - 1} \tag{15}$$

The Drucker–Prager hyperbolic function was used to determine the plastic flow of concrete. The flow potential function (G) is given in Eq. (16). The eccentricity, e, defined the rate at which the function approached asymptote. The uniaxial tensile strength was denoted by σ_{t0}. ψ was the dilation angle of p–q plane, which determined the direction of plastic strain increment.

$$G = \sqrt{(e\sigma_{t0}\tan\psi)^2 + \overline{q}^2} - \overline{p}\tan\psi \tag{16}$$

Concrete softening and stiffness degradation could cause convergence problem, particularly in implicit analysis that needed viscoplastic regularization. The Duvaut–Lions regularization method was used in the CDP model, which accounted for stress outside the yield surface. The viscoplastic strain rate tensor ($\dot{\varepsilon}_v^{pl}$) was presented in Eq. (17).

$$\dot{\varepsilon}_v^{pl} = \frac{1}{\mu}\left(\varepsilon^{pl} - \varepsilon_v^{pl}\right) \tag{17}$$

where μ is viscous parameter defining the relaxation of plastic strain.

The μ could be incorporated into the stiffness degradation variable, as shown in Eq. (18), allowing the damage to be computed with additional relaxation time. The viscoplastic model is given in Eq. (19).

$$\dot{d}_v = \frac{1}{\mu}(d - d_v) \tag{18}$$

$$\sigma = (d - d_v)D_o^{el} : \left(\varepsilon - \varepsilon_v^{pl}\right) \tag{19}$$

A sensitivity study was performed to calibrate the CDP parameters, which included dilation angle, eccentricity ratio of biaxial-to-uniaxial strength (σ_{b0}/σ_{c0}), ratio of tensile-to-compressive meridian (K_c) and viscosity parameter (μ), with details supplied in Appendix 3. Table 10 summarizes the CDP parameters used in this study.

4.4 Fatigue Loading Modelling

4.4.1 Geometry

The fatigue loading of concrete cubes (50 mm), which had previously been experimentally investigated by Ting et al. [49], was modelled here. Table 2 summarizes the details of test specimens. When the upper stress ratio (S_{max}) were 0.8, 0.85 and 0.9, the specimen was cyclically loaded to failure. At S_{max} of 0.3, 0.4 and 0.45, the specimens were loaded for 10,000 cycles. The loading frequency was 0.8 Hz, which corresponded to the experiment conditions. The S_{min} was held constant at 0.01. All specimens were plain concrete and were modelled as 3D deformable solid in ABAQUS.

4.4.2 Boundary Conditions

The loading and boundary conditions were modelled in accordance with the experiment [49]. The bottom surface of specimen was pinned by restraining the motion in x, y and z directions. Due to the loading plate restraint, only movement in z direction was allowed on the top surface. The specimen was initially pre-loaded with 1% static strength. The specimen was then subjected to cyclic loading with a triangular waveform [50].

4.4.3 Time Step and Loading Rate

Cyclic loading was modelled using dynamic explicit formulation. The explicit method, which evaluated the stress tensors element by element, avoided the need for global stiffness matrix and had less convergence issues [51]. The explicit solver required a low time step, which could cause instability if it exceeded the Courant–Friedrichs–Lewy time step [52]. Therefore, frequency analysis was performed to determine the appropriate loading rate. Figure 7 displays the failure of specimen in frequency analysis under compression crushing failure mode, with frequency of 18,617 Hz and time period of 5.37×10^{-5} s. However, the time was too short for the dynamic explicit solution, resulting in spike in kinetic energy. The acceptable kinetic-to-internal energy ratio was generally less than 0.05 [53]. The time period was thus increased by 100 times, and a time step of 0.011 s was used for one complete cycle of loading and unloading.

Table 2 Detail of test specimens for numerical modelling

Concrete type	Specimen label	Upper stress level, S_{max}	Loading cycle	Concrete mix	Exposure condition
T1	T1-S0.4	0.4	10,000	SM:(SF + FA)	Full immersion in 5% Na_2SO_4 (150 days)
	T1-S0.45	0.45	10,000		
T2	T2-S0.45	0.45	10,000	SM:(SF + FA)	E3 (150 days)
	T2-S0.8	0.8	Up to failure		
	T2-S0.85	0.85	Up to failure		
	T2-S0.0.9	0.9	Up to failure		
T3	T3-S0.8	0.8	Up to failure	LS:(SF + FA)	E3 (150 days)
	T3-S0.85	0.85	Up to failure		
	T3-S0.0.9	0.9	Up to failure		

4.4.4 Element Type and Meshing

The element type used was C3D8R, an 8-noded hexahedral element with reduced integration. The C3D8R was linear continuum element that modelled 3D solid material having large deformation. The C3D8R was used with hourglass control scheme to prevent excessive distortion in zero energy mode [52]. The integration points of C3D8R offered accurate estimation of stress and strain, which necessitated a smaller size element. A mesh sensitivity analysis was performed; the results of which were detailed in Appendix 3. A 10-mm mesh was used in this study, which was not too fine and was efficient in terms of computational time.

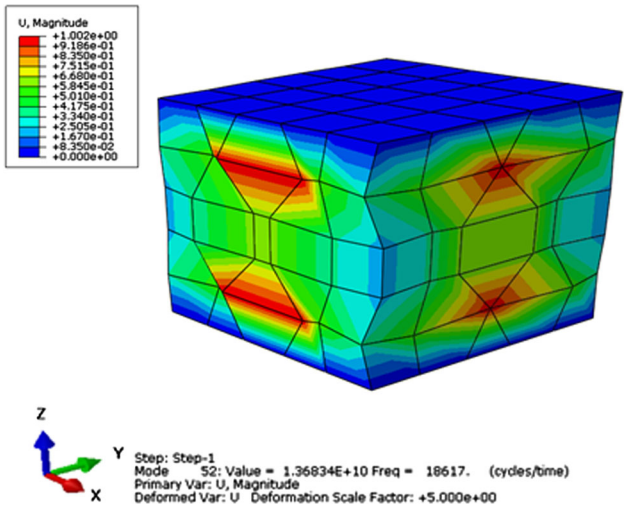

Fig. 7 Frequency analysis of specimen

5 Fatigue Loading Analysis and Discussion

5.1 Validation of Numerical Model

In this validation study, the numerical results in terms of failure mode, fatigue life, stress–strain curves and residual displacement were compared to the experimental results determined by Ting et al. [49].

5.1.1 Failure Mode and Fatigue Life

Figure 8a depicts the comparison of failure mode of concrete under cyclic loading between experiment and numerical model. The maximum plastic strain was used in the numerical analysis to illustrate the failure mode. The experimental results indicated that the specimen failed and cracks developed around the edge of concrete. The numerical results showed a similar failure mode, with the plastic strain localized at the center along specimen edge, demonstrating a crushing failure. Wang et al. [54] also showed that high-strength concrete exhibited brittle failure with significant superficial cracks initiated from specimen edge. Under compressive cyclic loading, the cracking mechanism typically began with internal micro-cracks surrounding the core bearing region, which were followed by exterior macro-cracks propagating towards the core [55].

Figure 8b compares the fatigue life (N_f) of specimens obtained through experiment and numerical analysis. The failure cycles determined by numerical analysis were all within the range determined in experiments. The numerical curve was slightly higher than the experimental curve, indicating that the concrete had longer fatigue life for a constant stress level. At S_{max} of 0.8 and 0.85, the concrete sustained longer loading cycles and failed close to the experimental fatigue life, but at higher S_{max} of 0.9, concrete in the experiment failed comparatively early. This might be caused by the increased sensitivity of experiment testing to actual loading conditions, as well as the inhomogeneous property of concrete, which resulted in variances of strength. Random defects such as micro-cracks and pores might cause discrepancies in results. Vicente et al. [56] reported that the fatigue life demonstrated a strong inversed relationship with pore

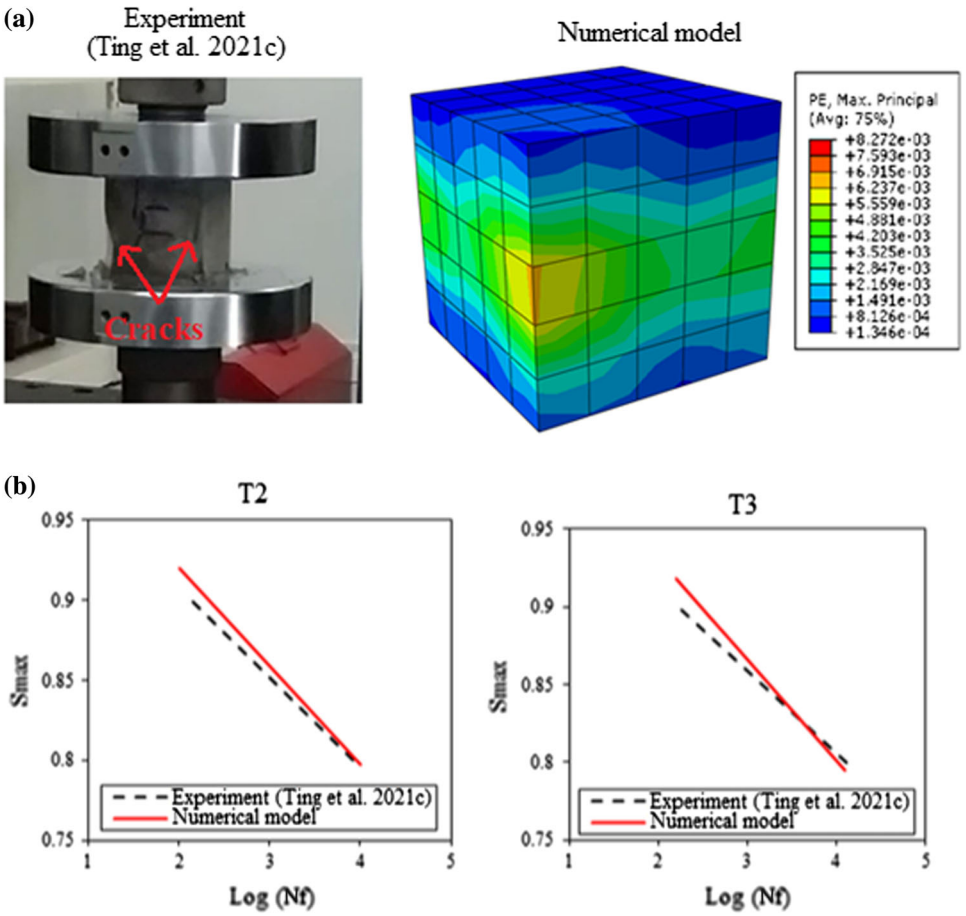

Fig. 8 **a** Crack patterns and **b** fatigue life in terms of S–N curves

volumes. Nonetheless, the numerical model could reasonably represent the shorter fatigue life of T2 than T3.

5.1.2 Fatigue Stress–Strain Curve

The stress–strain curves obtained from numerical analysis of T2-S0.8 and T3-S0.8 under cyclic loading are shown in Fig. 9. The curves of T2-S0.8 were plotted after 1, 4000 and 7000 loading cycles, and the curves of T3-S0.8 were plotted after 1, 5000 and 9000 loading cycles. The curves were compared to those determined from the experiment having similar failure cycle. As cycle number increased, the curves moved to the right, indicating a rise in residual strain. With increase in each loading cycle, the gradient of the stress–strain curve decreased and the elastic modulus degraded. The compressive cyclic loading generally deteriorated elastic modulus in two stages: early quasi-linear and ultimate fatigue [57]. In the first stage, the elastic modulus dropped linearly with the loading cycle, which might be caused by the formation of micro-cracks. In the later stage, micro-cracks bridged to create macro-cracks, resulting in considerable reduction in elastic modulus and then crushing failure. The fatigue strains of T2-S0.8 and T3-S0.8 measured in the experiment were

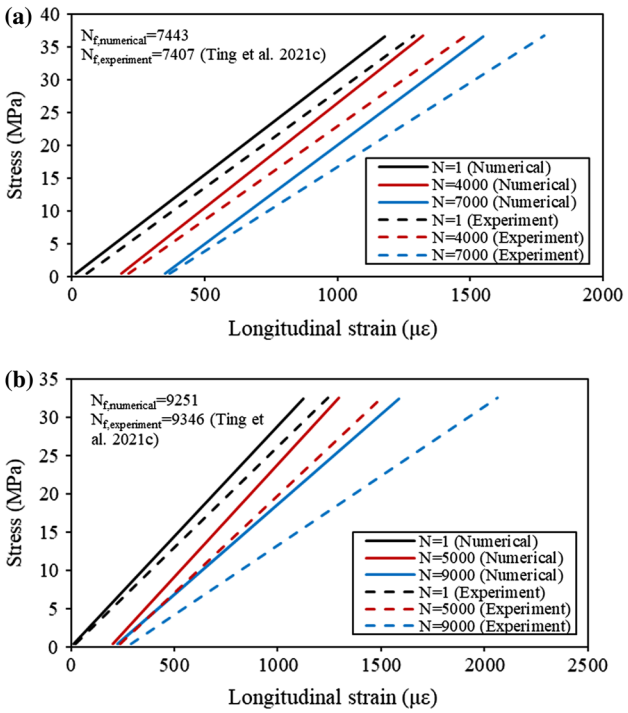

Fig. 9 Comparison of fatigue stress–strain curves: **a** T2-S0.8 and **b** T3-S0.8

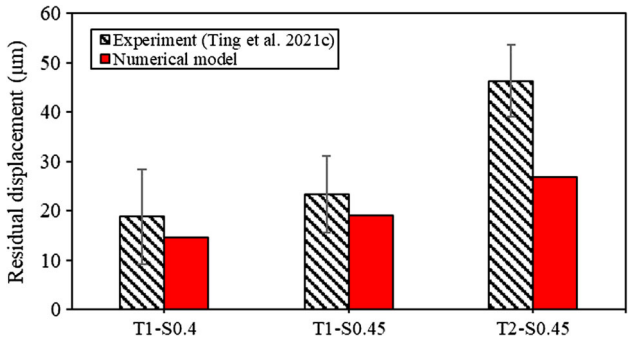

Fig. 10 Comparison of residual displacement

slightly greater than those calculated numerically, with differences of 9.1–14.8% and 10.5–30.1%, respectively.

5.1.3 Residual Displacement

Figure 10 compares the residual displacement of T1-S0.4, T1-S0.45 and T2-S0.45 after 10,000 loading cycles. The numerical residual displacement of T1 loaded at S_{max} of 0.4 and 0.45 was lower than the experimental values, with differences of 22.6% and 18.1%, respectively. Because the opening and closing of cracks under cyclic loading were modelled as stiffness recovery factor, the CDP model might overestimate the energy dissipation capability, resulting in reduced residual displacement [58]. One possible improvement was to increase the dilation angle in the CDP model, which would allow the material to expand more under loading. Besides, the difference between numerical and experimental displacements for T2-S0.45 subjected to sulphate attack was greater, with a discrepancy of 41.9%. The findings revealed that sulphate attack had significant influence on the prediction of residual displacement. Liao et al. [5] found that sulphate attack might increase the post-failure strain of concrete, especially after a long-term erosion period. The discrepancy might be due to the fact that the effect of sulphate attack on descending branch of stress–strain curve was not considered in the numerical model. However, the irregular deterioration of concrete caused by sulphate attack made determining post-failure strain difficult. Hence, it was suggested that future study collect comprehensive data using large numbers of strain gauge in order to improve model accuracy. Despite this limitation, the numerical model still fitted the experiment in terms of failure mode and fatigue life.

5.2 Feasibility Study of Model

The model validation showed that the numerical model corresponded well to the experiment. The model was used to investigate the influence of compressive strength (f_c'), lower stress level (S_{min}) and specimen size on the fatigue life of concrete, as shown in Table 3. In the numerical study, the S_{max} was kept constant at 0.9.

Table 3 Details of parametric study

Specimen label	f_c' (MPa)	S_{min}	Cube specimen size (mm)
P1	20	0.05	50
P2	50	0.05	50
P3	80	0.05	50
P4	80	0.1	50
P5	80	0.2	50
P6	80	0.05	100
P7	80	0.05	150

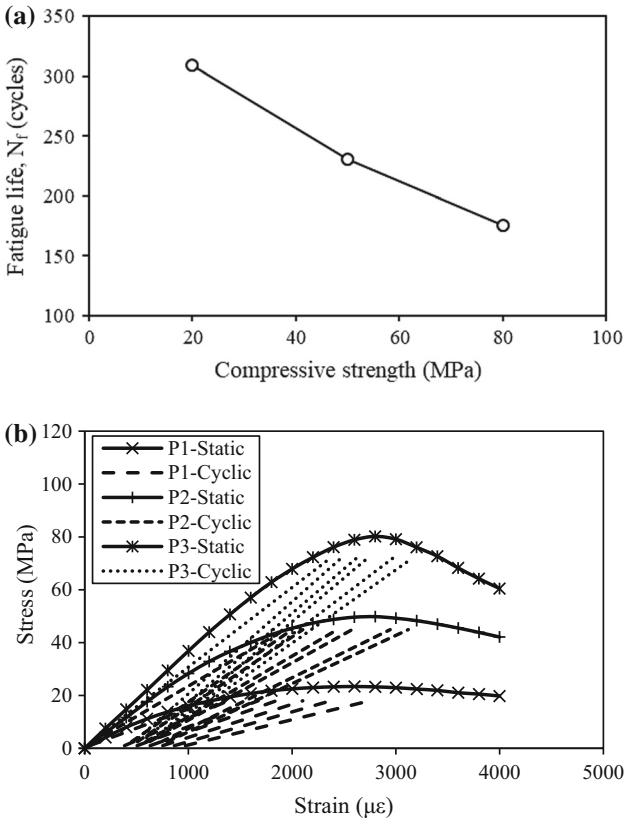

Fig. 11 Effect of compressive strength: **a** fatigue life and **b** fatigue stress–strain curve

5.2.1 Effect of Compressive Strength

Figure 11a shows the variation in fatigue life of concrete with compressive strengths. The fatigue life decreased from 309 to 231 cycles and 176 cycles, when strength was increased from 20 to 50 MPa and 80 MPa, respectively. This might be because greater strength concrete failures were more brittle and had lower failure strains, resulting in shorter fatigue life.

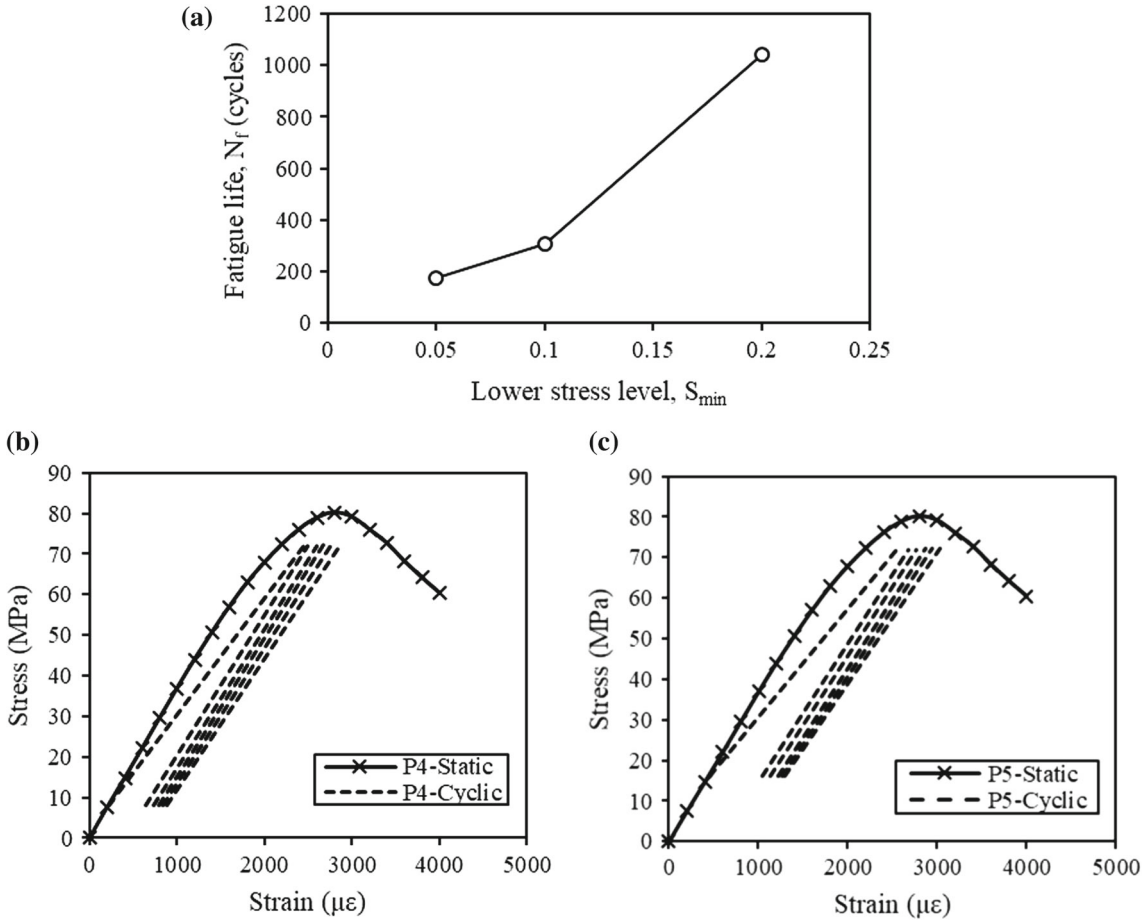

Fig. 12 **a** Effect of S_{min} on fatigue life, **b** P4 stress–strain curve, $S_{min} = 0.1$ and **c** P5 stress–strain curve, $S_{min} = 0.2$

Lantsoght et al. [59] demonstrated that the S–N curve for high-strength concrete was typically steeper and had lower fatigue life. High-strength concrete also exhibited a greater increase in fatigue strain than low strength concrete. This was evident in the fatigue stress–strain curves for P1, P2 and P3, as depicted in Fig. 11b. The elastic modulus decreased with increase in loading cycle and fatigue strain. The failure occurred for all concrete as the fatigue strain reached the descending branch of static curve. This might be attributed to the brittle behaviour of high strength, which demonstrated a lesser capacity to remain intact when inelastic strain grew.

5.2.2 Effect of Lower Stress Level

Figure 12a illustrates the influence of S_{min} on the fatigue life of concrete. Although S_{max} was as high as 0.9, increasing that S_{min} could considerably improve the fatigue resistance of concrete. When S_{min} was raised from 0.05 to 0.1 and 0.2, the fatigue life increased from 176 to 306 cycles and 1042 cycles, respectively. One explanation might be that the dynamic impact of cyclic loading decreased as the stress range between S_{max} and S_{min} decreased, resulting in less fatigue damage to the concrete. Hümme et al. [60] demonstrated that further increasing S_{min} to 0.4 caused almost negligible concrete damage, with no failures or superficial damages. Dineshkumar and Ramkumar [61] reported that cyclic loading with lower stress ranges might impede the crack initiation and propagation within concrete, enhancing fatigue resistance. Besides, specimen subjected to higher S_{min} also suffered less stiffness degradation, as indicated in the fatigue stress–strain curves in Fig. 12b and c. The failure strain under cyclic loading also rose with larger S_{min} and lower stress range, allowing the specimen to withstand greater deformation.

5.2.3 Effect of Specimen Size

Figure 13 depicts the effect of specimen size on fatigue life of concrete. The fatigue life increased marginally with the size of the specimen. For example, concrete with 50 mm, 100 mm and 150 mm sizes exhibited fatigue life of 176 cycles, 189 cycles and 203 cycles, respectively. The fatigue life increase might be attributed to an increase in element numbers in the finite element model as the specimen became

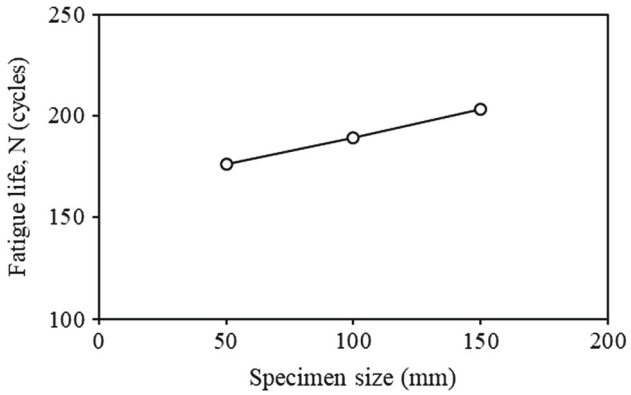

Fig. 13 Effect of specimen size on fatigue life

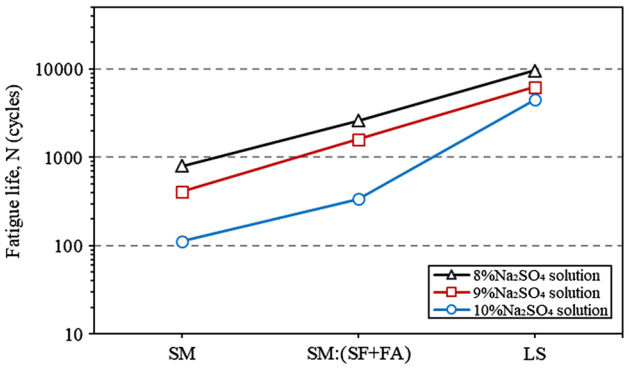

Fig. 14 Fatigue life of sulphate-attacked concrete in various salt solutions

larger. The increase in element mesh numbers could lead to an over-estimation of elastic stiffness in the dynamic explicit solver, which slightly improved the fatigue resistance [51]. The numerical findings contradicted the experimental results, which revealed that specimens of bigger size had shorter fatigue life [56, 62]. In actual condition, larger specimen had more inherent defects, such as cracks and pores, hence increasing probability of failure under cyclic loading. In the numerical analysis, this effect was not taken into consideration due to the difficulties in quantifying defects as they might vary substantially across specimens. Therefore, it was recommended that future study performed through extensive experimental investigations in order to acquire large-scale data on intrinsic defects, particularly for sulphate-attacked concrete. Despite this constraint, the influence of specimen size was marginal, with a maximum difference of 27 cycles.

5.3 Fatigue Life Prediction of Sulphate-Attacked Concrete

The fatigue life of concrete after sulphate attack was predicted using the numerical model. Three concrete types, which were LS, SM and SM:(SF + FA), were included in the numerical analysis. For comparison, all concrete types were given the same compressive strength of 60 MPa. The concrete was assumed to be exposed to wetting–drying environment with sulphate concentrations of 8%, 9% and 10% for 1 year. According to the ACI 215R-74 standard [63], the fatigue strength of concrete should be able to sustain 10×10^6 cycles loading at 55% of its compressive strength. This study therefore assessed the fatigue life of LS, SM and SM:(SF + FA) after deterioration, with S_{max} set at 33 MPa (55% of 60 MPa initial strength).

Figure 14 depicts the fatigue life of sulphate-attacked LS, SM and SM:(SF + FA). After 1 year of deterioration in 8% Na_2SO_4 solution, the fatigue life decreased significantly from the designed fatigue strength of 10×10^6 cycles to 798 cycles for SM, 2602 cycles for SM:(SF + FA) and 9649 cycles for LS. According to the constitutive relations, their compressive strengths fell by 32%, 35% and 37%, respectively, resulting in more fatigue damage and hence lower fatigue life. When the concentration of Na_2SO_4 solution was raised to 9% and 10%, the fatigue life of SM was reduced to 410 cycles and 113 cycles, respectively; SM:(SF + FA) had a fatigue life of 1603 cycles and 339 cycles, respectively, and LS had a fatigue life of 6216 cycles and 4470 cycles, respectively. The LS had a larger fatigue life than the SM due to its better performance in terms of stiffness, abrasion resistance and fatigue resistance. Furthermore, the porosity and permeability of LS were lower than that of SM, which was more resistant to sulphate attack [41]. On top of that, the results revealed that the use of FA and SF in concrete greatly increased the fatigue life. The concrete optimized with FA and SF displayed extended service life in the hostile marine environment.

However, this study highlights that the deterioration caused by sulphate attack considerably reduces concrete fatigue resistance, specifically fatigue life. Existing standards, such as ACI CODE-318-19(22) [64] and BS EN 197-1:2011 [65], provide specifications for cementitious binders against sulphate deterioration. ACI 215R-74 [63] and BS EN 1992-1-1:2004 [66] standards also address the concerns in the service environment for concrete subjected to cyclic loading. Therefore, to ensure structural durability, the combined effects of sulphate attack and cyclic loading should be considered in these standards when designing concrete structures exposed to sulphate-rich environments, especially coastal regions with high salinity and repeated cyclic wave action. Future research is recommended to include both experimental and numerical investigations covering a wide range of factors such as sulphate concentration and its interaction with other corrosive ions, loading stress levels and frequency, in order to improve the design guidelines.

6 Conclusions

This study investigated the fatigue resistance of sulphate-attacked concrete incorporated with silicomanganese slag, FA and SF. Experiments were performed to determine the damage constitutive relations of concrete in terms of compressive strength, tensile strength and sulphate intrusion. The fatigue performance of sulphate-attacked concrete was evaluated using the constitutive relations and CDP model. The following conclusions can be drawn:

1. The compressive and tensile strengths of sulphate-attacked concrete decreased over erosion time, with maximum strength decreases of 36–45% and 29–33%, respectively. Silicomanganese slag concrete exhibited 6.5–18% lower sulphate resistance than limestone concrete due to weaker aggregate bonding with cementitious binder. The sulphate resistance was compensated and improved by up to 7.3–13.8% with the addition of fly ash and silica fume.
2. Sulphate intrusion was expressed as integral area of SO_4^{2-} content over penetration depth of 0–20 mm. The rate of sulphate intrusion decreased exponentially over corrosion time, reaching 77.1–84.1% of the greatest values at 150 days. The compressive and tensile strength deteriorations were formulated as linear functions of SO_4^{2-} content, with R^2 values of. 0.93–0.94.
3. The constitutive relations and CDP model reasonably predicted the fatigue life of sulphate-attacked concrete, with 5.8–26.2% deviation from experiment. The numerical model measured the fatigue strain and residual displacement that were 9.1–30.1% and 18.1–41.9% lower than the experimental values, respectively.
4. Numerical analysis showed that increased concrete strength led to faster stiffness degradation, reducing fatigue resistance. Concrete subjected to higher S_{min} sustained more fatigue strain prior to failure, increasing fatigue life. The numerical model might overestimate elastic stiffness when specimen size increased.
5. Synergy of sulphate attack and cycle loading deteriorated the durability of concrete. A slight increase in sulphate solution concentration from 8 to 10% significantly reduced concrete fatigue life by 53.7–87% after 1 year, mostly due to strength and stiffness degradations.
6. Shortfalls existed in the proposed model that omitted concrete intrinsic defects and sulphate-induced post-failure characteristics. Future study is recommended to quantify the initial defects of concrete using X-ray computed tomography (CT) analysis as well as to evaluate the effect of sulphate attack on descending stress–strain curve using strain gauges.

Appendix 1

The comparison between experimental [49] and empirical compressive stress–strain curves is shown in Fig. 15.

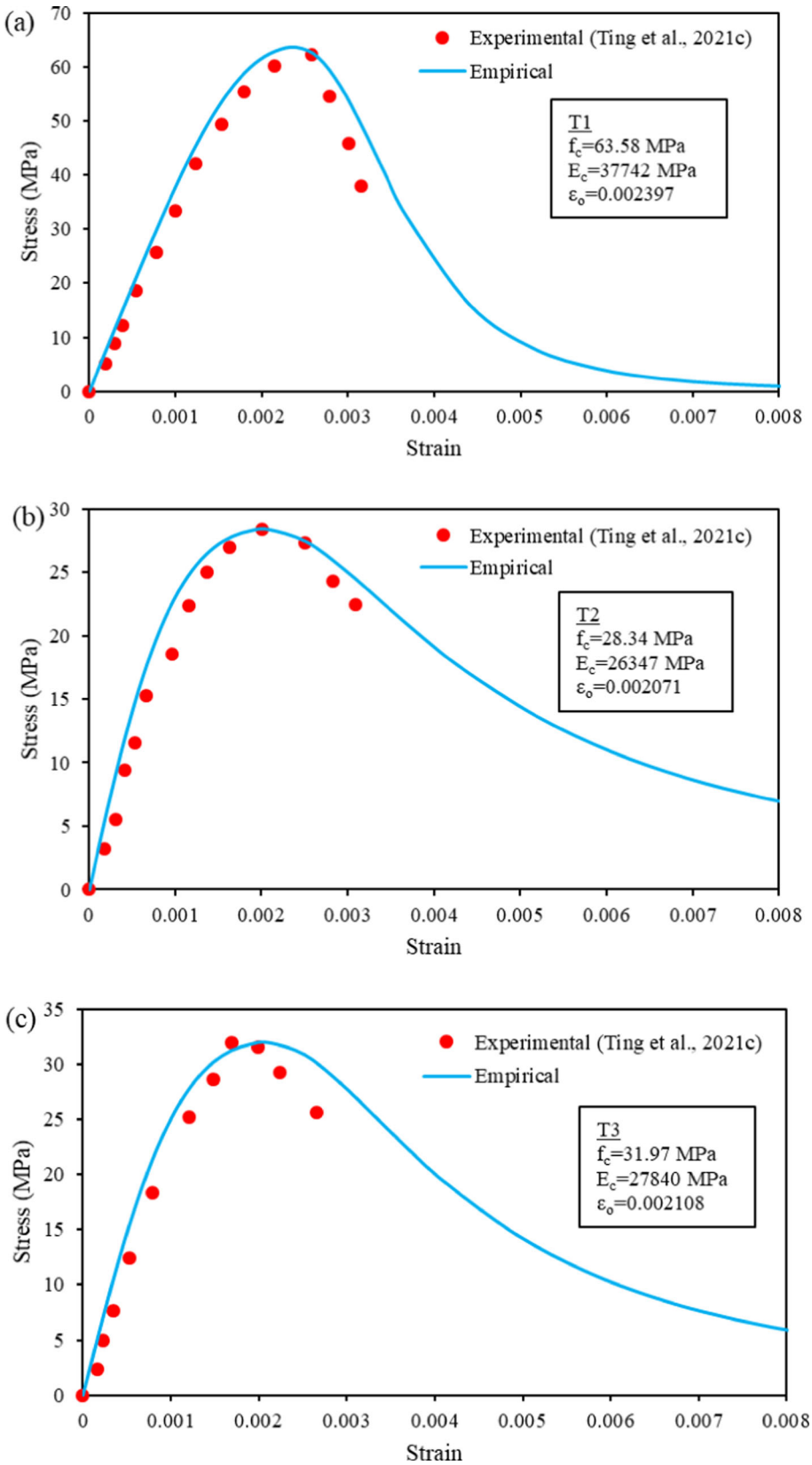

Fig. 15 Experimental and empirical compressive stress–strain curve: **a** T1, **b** T2 and **c** T3

Appendix 2

Tables 4, 5 and 6 present the compressive damage behaviour of T1, T2 and T3, and Tables 7, 8 and 9 summarize their tensile damage behaviour, all used in the CDP model.

Table 4 Compressive damage behaviour of T1

Compressive stress, σ_c (MPa)	Compressive damage, d_c	Inelastic strain, ε_{in}	Plastic strain, ε_{pl}
45.02	0	0	0
51.15	0	0.00005	0.00005
56.65	0	0.00014	0.00014
60.58	0	0.00028	0.00027
62.86	0	0.00046	0.00046
63.58	0	0.00068	0.00068
61.89	0.03	0.00098	0.00093
57.05	0.10	0.00136	0.00118
49.95	0.21	0.00181	0.00143
41.91	0.34	0.00228	0.00168
34.08	0.46	0.00274	0.00193
17.05	0.73	0.00395	0.00267
8.52	0.87	0.00492	0.00340
4.50	0.93	0.00577	0.00414

Table 5 Compressive damage behaviour of T2

Compressive stress, σ_c (MPa)	Compressive damage, d_c	Inelastic strain, ε_{in}	Plastic strain, ε_{pl}
18.02	0	0	0
20.60	0	0.00005	0.00005
23.49	0	0.00014	0.00014
26.94	0	0.00043	0.00043
27.78	0	0.00060	0.00060
28.34	0	0.00010	0.00010
25.11	0.11	0.00202	0.00190
22.44	0.21	0.00257	0.00235
17.39	0.39	0.00367	0.00325
13.63	0.52	0.00468	0.00412
10.86	0.62	0.00565	0.00498
8.81	0.69	0.00659	0.00585
7.28	0.74	0.00751	0.00672
5.21	0.82	0.00932	0.00845

Table 6 Compressive damage behaviour of T3

Compressive stress, σ_c (MPa)	Compressive damage, d_c	Inelastic strain, ε_{in}	Plastic strain, ε_{pl}
20.61	0	0	0
22.64	0	0.00003	0.00003
26.04	0	0.00012	0.00012
30.22	0	0.00039	0.00039
31.27	0	0.00056	0.00056
31.97	0	0.00096	0.00096
30.93	0.03	0.00141	0.00137
28.49	0.11	0.00190	0.00178
25.49	0.20	0.00242	0.00219
22.45	0.30	0.00294	0.00260
14.97	0.53	0.00445	0.00384
9.15	0.71	0.00632	0.00550
7.37	0.77	0.00722	0.00633
5.05	0.84	0.00896	0.00800

Table 7 Tensile damage behaviour of T1

Tensile stress, σ_t (MPa)	Tensile damage, d_c	Inelastic strain, ε_{in}	Plastic strain, ε_{pl}
5.27	0	0	0
4.06	0.23	0.00006	0.00003
3.05	0.42	0.00029	0.00024
2.37	0.55	0.00045	0.00038
2.00	0.62	0.00058	0.00050
1.26	0.76	0.00083	0.00073
0.53	0.90	0.00109	0.00097

Table 8 Tensile damage behaviour of T2

Tensile stress, σ_t (MPa)	Tensile damage, d_c	Inelastic strain, ε_{in}	Plastic strain, ε_{pl}
2.89	0	0	0
2.23	0.23	0.00005	0.00002
1.67	0.42	0.00022	0.00018
1.30	0.55	0.00034	0.00029
1.10	0.62	0.00043	0.00038
0.69	0.76	0.00063	0.00055
0.29	0.90	0.00082	0.00073

Table 9 Tensile damage behaviour of T3

Tensile stress, σ_t (MPa)	Tensile damage, d_c	Inelastic strain, ε_{in}	Plastic strain, ε_{pl}
3.17	0	0	0
2.44	0.23	0.00005	0.00002
1.83	0.42	0.00023	0.00019
1.43	0.55	0.00035	0.00030
1.20	0.62	0.00045	0.00039
0.76	0.76	0.00066	0.00058
0.32	0.90	0.00086	0.00077

Appendix 3

The CDP parameters were calibrated against test result under static loading as shown in Fig. 16. The effect of viscoplasticity regularization was negligible in dynamic explicit formulation; hence, μ of 0 was used [52]. The dilation angle defined the plastic strain growth caused by shear stress up to the critical point. Concrete was brittle and generally had dilation angle ranging from 31° to 42° [51]. Figure 16a showed that the peak stress and strain increased as the dilation angle increased from 20° to 40°. A greater dilation angle indicated that the material was more ductile. The stress–strain curve with dilation angle of 40° fitted the experimental results well. The eccentricity determined the rate at which hyperbolic Drucker–Prager flow potential approached its asymptote. As depicted in Fig. 16b, the eccentricity had negligible effect on the stress–strain response. Hence, eccentricity was chosen as the default value of 0.1. The K_c was the tensile-to-compressive meridian ratio on the deviatory plane. According to the Drucker–Prager yield criterion, K_c varied from 0.667 to 1, with 1 referring to circular deviatory plane failure. As shown in Fig. 16c, the peak stress and strain significantly decreased with an increase in K_c value. Based on the sensitivity study, K_c value of 0.667 was selected. The σ_{b0}/σ_{c0} specified the failure state of concrete under biaxial compression. The stress–strain curve with σ_{b0}/σ_{c0} of 1.16 was selected since it best fitted to the experimental results (Fig. 16d).

A mesh sensitivity study was performed using T2 specimen as shown in Fig. 17. The peak stress generally decreased with mesh size. The 16 mm- and 12.5-mm meshes were too

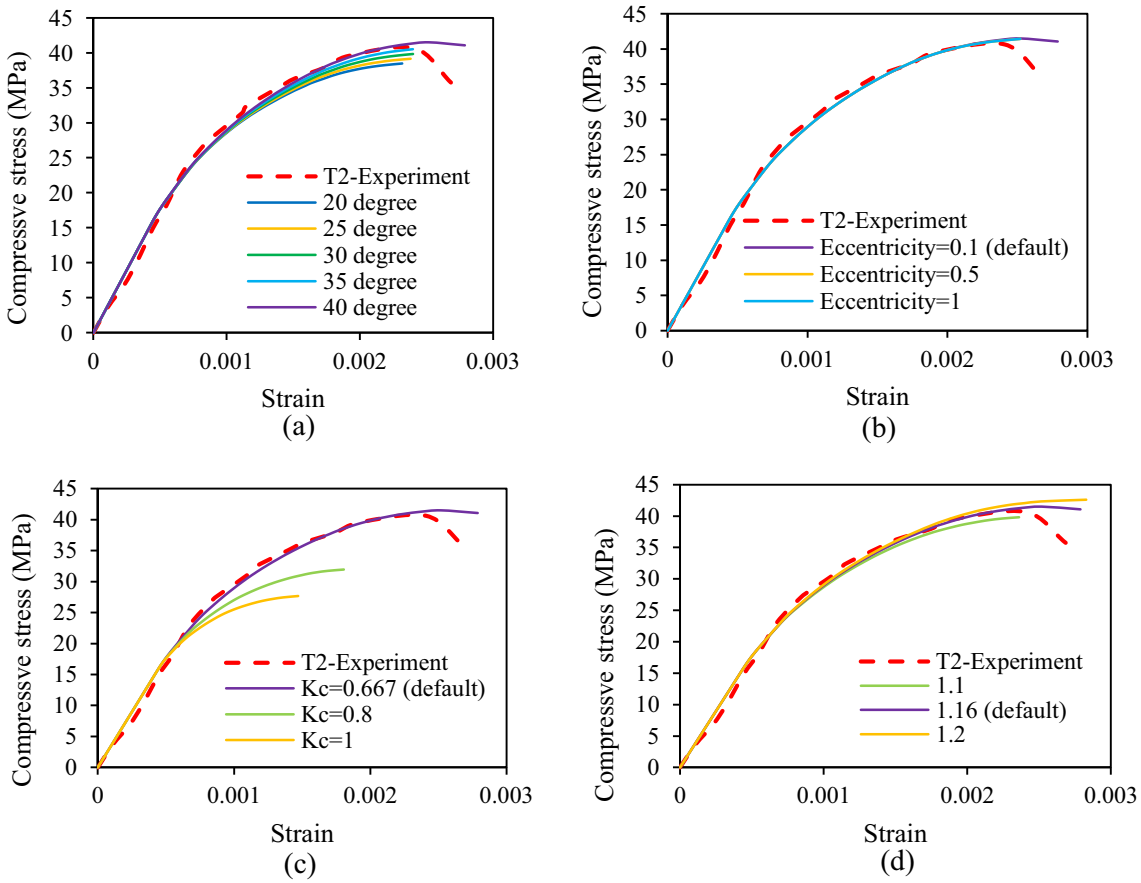

Fig. 16 Calibration of CDP parameters: **a** dilation angle, **b** eccentricity, **c** K_c value and **d** σ_{b0}/σ_{c0} ratio

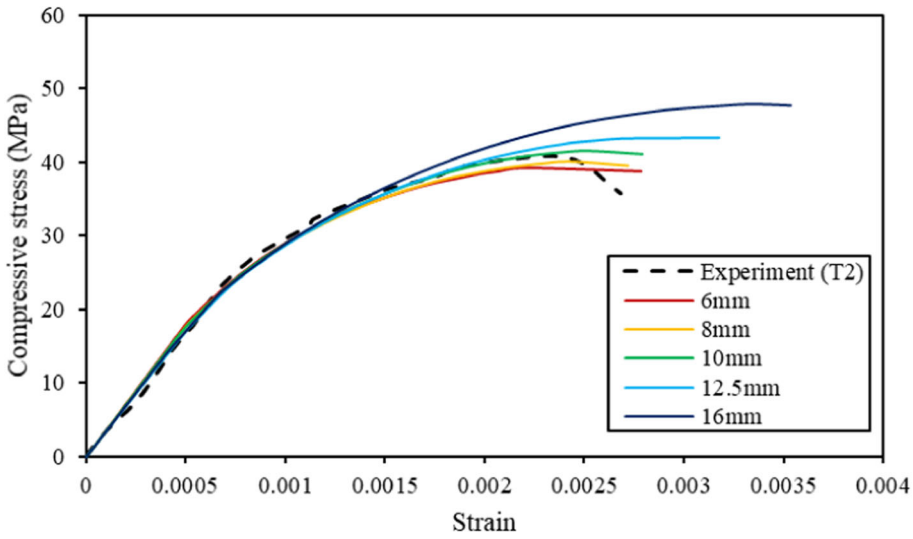

Fig. 17 Mesh sensitivity study

Table 10 Calibrated CDP parameters

CDP parameter	Calibrated value
Dilation angle	40°
Eccentricity	0.1
K_c	0.667
σ_{b0}/σ_{c0}	1.16
μ	0

coarse, causing peak stress to be overestimated. The peak stress in 10 mm mesh was comparable to the experimental result, with a 2.1% difference. Further decrease in mesh size to 8 mm and 6 mm had minimal effects. Therefore, an optimum mesh size of 10 mm was selected.

See Table 10.

Acknowledgements The authors gratefully acknowledge the financial support provided by Novakey Developer Sdn. Bhd. during the initial stages of this project. The authors would also like to thank Curtin University, Malaysia, for providing research facilities and assistance throughout the project.

Funding Open Access funding enabled and organized by CAUL and its Member Institutions.

References

1. Neville, A.: The confused world of sulfate attack on concrete. Cem. Concr. Res. **34**(8), 1275–1296 (2004)
2. Idiart, A.E.; López, C.M.; Carol, I.: Chemo-mechanical analysis of concrete cracking and degradation due to external sulfate attack: a meso-scale model. Cement Concr. Compos. **33**(3), 411–423 (2011)
3. Ma, B.; Wang, Y.; Fu, H.: Effect of rice husk ash on the thaumasite form of sulfate attack of cement-based materials. Arab. J. Sci. Eng. **39**, 8517–8524 (2014)
4. Rozière, E.; Loukili, A.; El Hachem, R.; Grondin, F.: Durability of concrete exposed to leaching and external sulphate attacks. Cem. Concr. Res. **39**(12), 1188–1198 (2009)
5. Liao, K.-X.; Zhang, Y.-P.; Zhang, W.-P.; Wang, Y.; Zhang, R.-L.: Modeling constitutive relationship of sulfate-attacked concrete. Constr. Build. Mater. **260**, 119902 (2020)
6. Ikumi, T.; Segura, I.: Numerical assessment of external sulfate attack in concrete structures. A review. Cem. Concr. Res. **121**, 91–105 (2019)
7. Cheng, H.; Liu, T.; Zou, D.; Zhou, A.: Compressive strength assessment of sulfate-attacked concrete by using sulfate ions distributions. Constr. Build. Mater. **293**, 123550 (2021)
8. Jiang, L.; Niu, D.: Study of deterioration of concrete exposed to different types of sulfate solutions under drying–wetting cycles. Constr. Build. Mater. **117**, 88–98 (2016)
9. Zhang, Z.; Jin, X.; Luo, W.: Long-term behaviors of concrete under low-concentration sulfate attack subjected to natural variation of environmental climate conditions. Cem. Concr. Res. **116**, 217–230 (2019)
10. Tang, J.; Cheng, H.; Zhang, Q.; Chen, W.; Li, Q.: Development of properties and microstructure of concrete with coral reef sand under sulphate attack and drying–wetting cycles. Constr. Build. Mater. **165**, 647–654 (2018)
11. Gao, J.; Yu, Z.; Song, L.; Wang, T.; Wei, S.: Durability of concrete exposed to sulfate attack under flexural loading and drying–wetting cycles. Constr. Build. Mater. **39**, 33–38 (2013)

12. Yu, X.-T.; Chen, D.; Feng, J.-R.; Zhang, Y.: Behavior of mortar exposed to different exposure conditions of sulfate attack. Ocean Eng. **157**, 1–12 (2018)
13. De Souza, D.J.; Sanchez, L.F.M.; Hoppe Filho, J.; Medeiros, M.H.F.: Development of a durability indicator to forecast the efficiency of preventive measures against external sulphate attack. Cem. Concr. Compos. **145**, 105349 (2024)
14. Mallek, J.; Omikrine-Metalssi, O.; Loulizi, A.; Daoud, A.: Durability of self-compacting rubberized concrete exposed to external sulphate attack. Case Stud. Constr. Mater. **20**, e02730 (2024)
15. Chen, F.; Gao, J.; Qi, B.; Shen, D.; Li, L.: Degradation progress of concrete subject to combined sulfate-chloride attack under drying–wetting cycles and flexural loading. Constr. Build. Mater. **151**, 164–171 (2017)
16. Zhang, J.; Sun, M.; Hou, D.; Li, Z.: External sulfate attack to reinforced concrete under drying–wetting cycles and loading condition: numerical simulation and experimental validation by ultrasonic array method. Constr. Build. Mater. **139**, 365–373 (2017)
17. Fu, C.; Ye, H.; Jin, X.; Yan, D.; Jin, N.; Peng, Z.: Chloride penetration into concrete damaged by uniaxial tensile fatigue loading. Constr. Build. Mater. **125**, 714–723 (2016)
18. Dandapat, R.; Deb, A.: A probability based model for the erosive wear of concrete by sediment bearing water. Wear **350**, 166–181 (2016)
19. Chen, Y.; Gao, J.; Tang, L.; Li, X.J.C.: Resistance of concrete against combined attack of chloride and sulfate under drying–wetting cycles. Construct. Build. Mater. **106**, 650–658 (2016)
20. Burcharth, H.F.: Fatigue in breakwater concrete armour units. In: Coastal Engineering Proceedings, pp. 174 (1984)
21. Haritos, N.: Introduction to the analysis and design of offshore structures: an overview. Electron. J. Struct. Eng. **1**, 55–65 (2007)
22. Long, T.; Zhang, H.; Chen, Y.; Li, Z.; Xu, J.; Shi, X.; Wang, Q.: Effect of sulphate attack on the flexural fatigue behaviour of fly ash–based geopolymer concrete. J. Strain Anal. Eng. Des. **53**(8), 711–718 (2018)
23. Biswas, S.; Verma, G.K.; Sengupta, P.: Seismic fragility of corroded reinforced concrete highway bridges. In: Current Perspectives and New Directions in Mechanics, Modelling and Design of Structural Systems, pp. 228–232. CRC Press (2022)
24. Flansbjer, M.; Lindqvist, J.-E.; Johansson, G.; Löfgren, M.: Mechanical behaviour of concrete piles affected by sulphate attack. In: Proceeding of fib Symposium: Concrete Structures for Sustainable Community, pp. 389–392 (2012)
25. Wu, J.Y.; Li, J.; Faria, R.: An energy release rate-based plastic-damage model for concrete. Int. J. Solids Struct. **43**(3–4), 583–612 (2006)
26. Lee, J.; Fenves, G.L.: Plastic-damage model for cyclic loading of concrete structures. J. Eng. Mech. **124**(8), 892–900 (1998)
27. Azadi Kakavand, M.R.; Taciroglu, E.: An enhanced damage plasticity model for predicting the cyclic behavior of plain concrete under multiaxial loading conditions. Front. Struct. Civ. Eng. **14**(6), 1531–1544 (2020)
28. Minh, H.-L.; Khatir, S.; Wahab, M.A.; Cuong-Le, T.: A concrete damage plasticity model for predicting the effects of compressive high-strength concrete under static and dynamic loads. J. Build. Eng. **44**, 103239 (2021)
29. Murthy, A.R.; Karihaloo, B.L.; Rani, P.V.; Priya, D.S.: Fatigue behaviour of damaged RC beams strengthened with ultra high performance fibre reinforced concrete. Int. J. Fatigue **116**, 659–668 (2018)
30. Wang, D.; Zhou, X.; Meng, Y.; Chen, Z.: Durability of concrete containing fly ash and silica fume against combined freezing-thawing and sulfate attack. Constr. Build. Mater. **147**, 398–406 (2017)
31. Singh, D.; Singla, S.: Effect of chloride and sulphate attack in concrete containing biomass ash and silica fumes. Iran. J. Sci. Technol. Trans. Civil Eng. (2024). https://doi.org/10.1007/s40996-023-01332-2
32. Zou, Y.-X.; Zuo, X.-B.; Zhang, H.-L.; Wang, S.-Q.: Influence of fly ash and chlorides on the behavior of sulfate attack in blended cement pastes. Constr. Build. Mater. **394**, 132231 (2023)
33. Patil, A.V.; Pande, A.M.: Behaviour of silico manganese slag manufactured aggregate as material for road and rail track construction. Adv. Mater. Res. **255**, 3258–3262 (2011)
34. Choi, H.-B.; Kim, J.M.: Properties of silicon manganese slag as an aggregate for concrete depending on cooling conditions. J. Mater. Cycles Waste Manage. **22**(4), 1067–1080 (2020)
35. Ting, M.Z.Y.; Wong, K.S.; Rahman, M.E.; Selowarajoo, M.: Prediction model for hardened state properties of silica fume and fly ash based seawater concrete incorporating silicomanganese slag. J.f Build. Eng. **41**, 102356 (2021)
36. ASTM: Standard Test Method for Compressive Strength of Cylindrical Concrete Specimens. ASTM C39/C39M-19. PA:ASTM, West Conshohocken. (2019)
37. ASTM: Standard Test Method for Splitting Tensile Strength of Cylindrical Concrete Specimens. ASTM C496/C496M-17. PA:ASTM, West Conshohocken (2017)
38. ASTM: Standard Test Methods for Chemical Analysis of Hydraulic Cement. ASTM C114-18. PA:ASTM, West Conshohocken (2018)
39. Nath, S.K.; Randhawa, N.S.; Kumar, S.: A review on characteristics of silico-manganese slag and its utilization into construction materials. Resour. Conserv. Recycl. **176**, 105946 (2022)
40. Xing, Z.; Han, F.; Tian, J.; Xu, Z.; Wang, J.; Liu, T.; Zheng, B.; Huang, J.: Preparation and characterization of the functional properties of synthetic aggregates from silico-manganese slag. Materials **14**(23), 7303 (2021)
41. Ting, M.Z.Y.; Wong, K.S.; Rahman, M.E.; Joo, M.S.: Mechanical and durability performance of marine sand and seawater concrete incorporating silicomanganese slag as coarse aggregate. Constr. Build. Mater. **254**, 119195 (2020)
42. El-Sayed, T.A.; Shaheen, Y.B.I.: Flexural performance of recycled wheat straw ash-based geopolymer RC beams and containing recycled steel fiber. Structures **28**, 1713–1728 (2020)
43. El-Sayed, T.A.: Flexural behavior of RC beams containing recycled industrial wastes as steel fibers. Constr. Build. Mater. **212**, 27–38 (2019)
44. Vishwakarma, R.J.; Kumari, P.; Morkhade, S.G.; Bahekar, P.V.: Engineering properties of two-stage concrete: a critical review. Mater. Today: Proc. **77**, 729–733 (2023)
45. Yang, K.-H.; Mun, J.-H.; Cho, M.-S.; Kang, T.H.K.: Stress-strain model for various unconfined concretes in compression. ACI Struct. J. **111**(4), 819 (2014)
46. Nayal, R.; Rasheed, H.A.: Tension stiffening model for concrete beams reinforced with steel and FRP bars. J. Mater. Civ. Eng. **18**(6), 831–841 (2006)
47. Wahalathantri, B.; Thambiratnam, D.; Chan, T.; Fawzia, S.: A material model for flexural crack simulation in reinforced concrete elements using ABAQUS. In: Proceedings of the First International Conference on Engineering, Designing and Developing the Built Environment for Sustainable Wellbeing, pp. 260–264 (2011)
48. Lubliner, J.; Oliver, J.; Oller, S.; Oñate, E.: A plastic-damage model for concrete. Int. J. Solids Struct. **25**(3), 299–326 (1989)
49. Ting, M.Z.Y.; Wong, K.S.; Rahman, M.E.; Joo, M.S.: Cyclic compressive behavior of limestone and silicomanganese slag concrete subjected to sulphate attack and wetting–drying action in marine environment. J. Build. Eng. **44**, 103357 (2021)
50. Rao, A.S.; Lepech, M.D.; Kiremidjian, A.S.; Sun, X.-Y.: Simplified structural deterioration model for reinforced concrete bridge piers under cyclic loading. Struct. Infrastruct. Eng. **13**(1), 55–66 (2017)

51. Genikomsou, A.S.; Polak, M.A.: Finite element analysis of punching shear of concrete slabs using damaged plasticity model in ABAQUS. Eng. Struct. **98**, 38–48 (2015)
52. Abaqus: Abaqus Analysis User's Manual (V6.14 ed.). Machinery Industry Press (2012)
53. Coelho, A.M.G.; Mottram, J.T.; Harries, K.A.: Finite element guidelines for simulation of fibre-tension dominated failures in composite materials validated by case studies. Compos. Struct. **126**, 299–313 (2015)
54. Wang, S.; Xu, L.; Yin, C.; Chen, Z.; Chi, Y.: Experimental investigation on the damage behavior of ultra-high performance concrete subjected to cyclic compression. Compos. Struct. **267**, 113855 (2021)
55. Zhou, M.; Liao, J.; An, L.; Deng, W.; Hassanein, M.F.; Yu, Z.: Analysis of stress-induced cracks in concrete and mortar under cyclic uniaxial compression. Constr. Build. Mater. **187**, 652–664 (2018)
56. Vicente, M.A.; González, D.C.; Mínguez, J.; Tarifa, M.A.; Ruiz, G.; Hindi, R.: Influence of the pore morphology of high strength concrete on its fatigue life. Int. J. Fatigue **112**, 106–116 (2018)
57. Ting, M.Z.Y.; Ting, T.Z.H.: Deterioration of structural shear connectors in steel-concrete composite exposed to hostile service environments. J. Build. Eng. **73**, 106690 (2023)
58. Xiao, K.; Zhang, Q.; Jia, B.: Cyclic behavior of prefabricated reinforced concrete frame with infill slit shear walls. Front. Struct. Civ. Eng. **10**(1), 63–71 (2016)
59. Lantsoght, E.O.L.; van der Veen, C.; de Boer, A.: Proposal for the fatigue strength of concrete under cycles of compression. Constr. Build. Mater. **107**, 138–156 (2016)
60. Hümme, J.; von der Haar, C.; Lohaus, L.; Marx, S.: Fatigue behaviour of a normal-strength concrete–number of cycles to failure and strain development. Struct. Concr. **17**(4), 637–645 (2016)
61. Dineshkumar, R.; Ramkumar, S.: Review paper on fatigue behavior of reinforced concrete beams. Mater. Today: Proc. **21**, 19–23 (2020)
62. Fládr, J.; Bílý, P.: Specimen size effect on compressive and flexural strength of high-strength fibre-reinforced concrete containing coarse aggregate. Compos. B Eng. **138**, 77–86 (2018)
63. ACI: Considerations for Design of Concrete Structures Subjected to Fatigue Loading. ACI 215R-74. MI: ACI, Farmington Hills (1997)
64. ACI: Building Code Requirements for Structural Concrete and Commentary. ACI CODE-318-19(22). Farmington Hills: American Concrete Institute (2022)
65. Standard, B.: Cement—Composition, Specifications and Conformity Criteria for Common Cements. BS EN 197-1:2011. London: BSI (2011)
66. Standard, B.: Eurocode 2: Design of concrete structures - General rules and rules for buildings. BS EN 1992-1-1:2004. London: BSI (2004)